ACADEMIC
PRESS

Available online at www.sciencedirect.com

SCIENCE DIRECT®

Journal of Computational Physics 186 (2003) 397–425

JOURNAL OF
COMPUTATIONAL
PHYSICS

www.elsevier.com/locate/jcp

A three-dimensional spectral element model for the solution of the hydrostatic primitive equations

M. Iskandarani [a,*], D.B. Haidvogel [b], J.C. Levin [b]

[a] *Rosenstiel School of Marine and Atmospheric Science, University of Miami, 4600 Rickenbacker Causeway, Miami, FL 33149, USA*
[b] *Institute of Marine and Coastal Science, Rutgers University, 71 Dudley Road, New Brunswick, NJ 08901-0231, USA*

Received 3 January 2001; received in revised form 14 February 2002; accepted 19 December 2002

Abstract

We present a spectral element model to solve the hydrostatic primitive equations governing large-scale geophysical flows. The highlights of this new model include unstructured grids, dual *h–p* paths to convergence, and good scalability characteristics on present day parallel computers including Beowulf-class systems. The behavior of the model is assessed on three process-oriented test problems involving wave propagation, gravitational adjustment, and nonlinear flow rectification, respectively. The first of these test problems is a study of the convergence properties of the model when simulating the linear propagation of baroclinic Kelvin waves. The second is an intercomparison of spectral element and finite-difference model solutions to the adjustment of a density front in a straight channel. Finally, the third problem considers the comparison of model results to measurements obtained from a laboratory simulation of flow around a submarine canyon. The aforementioned tests demonstrate the good performance of the model in the idealized/process-oriented limits.

Keywords: Spectral element; Hydrostatic primitive equations; Ocean model

---

1. Introduction

We describe a new spectral element model for the solution of the three-dimensional hydrostatic primitive equations, i.e., the Navier–Stokes equations as modified by the assumptions of hydrostatic balance and the Boussinesq approximation. The spectral element method offers several attractive properties for geophysical simulations: geometrical flexibility with a spatial discretization based on unstructured grids, high-order convergence rates, and dense computations at the elemental level leading to extremely good scalability characteristics on parallel computers. Our aim is to capitalize on these properties to obtain highly accurate simulations of regional, basin-scale, and (eventually) global circulation processes.

---

[*] Corresponding author.

E-mail addresses: miskandarani@rsmas.miami.edu (M. Iskandarani), dale@imcs.rutgers.edu (D.B. Haidvogel), julia@imcs.rutgers.edu (J.C. Levin).

0021-9991/03/$ - see front matter © 2003 Elsevier Science B.V. All rights reserved.
doi:10.1016/S0021-9991(03)00025-1

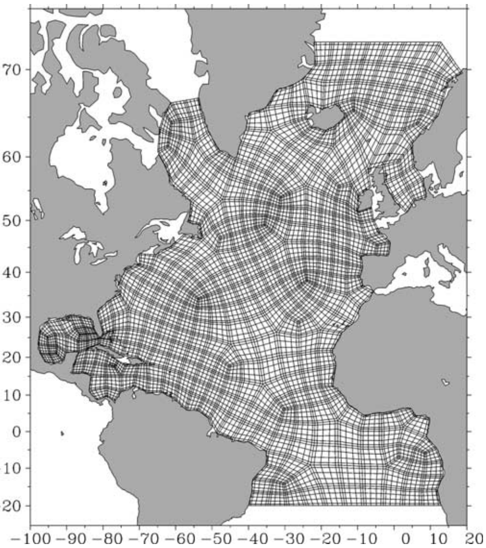

Fig. 1. Surface slice of a sample 3D spectral element grid showing the elements along with the Gauss–Lobatto points ($N = 6$). The elemental partition is evident since the Gauss–Lobatto points cluster near the element's edge. The grid holds 388 elements, and has an average grid spacing of 3/4°.

The spectral element method is an *h–p* type finite element method that approximates the solution within each quadrilateral element with a high-order polynomial. The unstructured nature of its elemental grid permits a better geometrical description of complex geometries (e.g., ocean basins), easily accommodates spatially variable resolution to resolve regionally localized, fine-scale processes (such as western boundary currents like the Gulf Stream), and therefore enables multi-scale simulations within the frame-work of a single model. (Fig. 1 shows an example of a spectral element grid encompassing the North Atlantic basin.) The spectral element method also offers a dual approach to convergence: algebraic (via elemental grid refinement) and exponential (via increase in the order of intra-element interpolation). The combination of spatially variable resolution, rapid convergence to the true solution, and excellent scalability on parallel systems are especially advantageous for high-accuracy simulation of fine-scale geophysical processes.

Ma [16] presented the first application of the spectral element method to the simulation of two-dimensional geophysical flows. Iskandarani et al. [10] modified her procedure and staggered the pressure and velocity grids in order to suppress spurious pressure modes. The model in [10] is the two-dimensional precursor to the one presented herein, and solves the depth-integrated form of the three-dimensional equations: the shallow water equations. This model has been tested thoroughly and various applications can be found in [4,5,8,13,27]. The model's scalability and performance on parallel machines is demonstrated in [6]. More recently, Levin et al. [14] enhanced the model with a mortaring capability to allow the use of multiple spectral expansions in different regions of the domain.

Taylor developed a spectral element atmospheric model (SEAM) capable of handling the full spherical domain by regularizing the polar singularity [20,21]. The two-dimensional version of the atmospheric model was validated using the standard spherical test suite of Williamson et al. [25]. This validation includes comparison to analytical and model results and confirms that spectral elements have most of the advantages of spherical harmonics including exponential converge under *p*-refinement (i.e., increasing the degree N of the interpolating polynomial). Taylor and co-workers [20] have also demonstrated the efficiency of SEAM for the three-dimensional primitive equations; their model relies on isobaric coordinates in the vertical and on finite differences for the vertical discretization.

All the models mentioned above use quadrilateral elements for the spatial discretization. Wingate has devised a triangular spectral element method for the shallow water equations [26]. In addition, Taylor and Wingate have explored triangular spectral elements that rely on Lagrange interpolants to approximate the solution. Their method is described in [22,23,27].

Here, we present the extension of the two-dimensional ocean model to three dimensions. In particular, we emphasize several key points that are of crucial importance in geophysical modeling. These issues are: accurate treatment of underlying bathymetry, calculation of the baroclinic pressure gradients, and the calculation of the depth-integrated (barotropic) component of the flow when the model is allowed to support free-surface waves.

The plan for the rest of the paper is as follows. Section 2 lists the equations and boundary conditions governing the flows of interest. Sections 3 and 4 discuss the changes to these equations arising due to the mapping of the moving free surface to a steady computational domain and the variational formulation of the resulting equations. Sections 5 and 6 introduce the spatial and temporal discretizations of the equations, respectively. Section 7 summarizes the solution procedure and discusses the calculation of the baroclinic pressure terms.

Convergence properties of the resulting model are assessed in Section 9 in which we consider the propagation of a baroclinic Kelvin wave along a periodic channel of constant depth. Section 10 investigates the ability of the model to deal with the adjustment of density fronts in a straight channel. The last test case (Section 11) compares the spectral element model results to laboratory measurements of a flow around a submarine canyon; we focus in particular on recent numerical experiments (part of a sensitivity study) that show improved agreement between model and experiment over results shown in [17]. Section 12 focusses on the scalability issues and presents timings performed on the Cray-T3E. Finally, Section 13 summarizes and discusses our experience with the spectral element model.

2. Equations of motion

The equations governing large-scale geophysical flows are the hydrostatic Boussinesq primitive equations:

$$\frac{D\mathbf{u}}{Dt} + \mathbf{f}\times\mathbf{u} + g\nabla\zeta + \nabla p = \nabla\cdot(\alpha\nabla\mathbf{u}) + \frac{\partial}{\partial z}\left(\nu\frac{\partial\mathbf{u}}{\partial z}\right), \tag{1}$$

$$\frac{\partial p}{\partial z} = -g\frac{\rho}{\rho_0}, \tag{2}$$

$$\nabla\cdot\mathbf{u} + \frac{\partial w}{\partial z} = 0 \tag{3}$$

supplemented (e.g., for the ocean) with conservation equations for temperature and salt concentration, and an equation of state linking density to temperature and salinity:

$$\frac{D}{Dt}\begin{pmatrix}T\\S\end{pmatrix} = \nabla\cdot\left[\alpha_t\nabla\begin{pmatrix}T\\S\end{pmatrix}\right] + \frac{\partial}{\partial z}\left[\nu_t\frac{\partial}{\partial z}\begin{pmatrix}T\\S\end{pmatrix}\right], \tag{4}$$

$$\rho = \rho(T,S). \tag{5}$$

Here, $\mathbf{u}$ is the horizontal velocity vector; w, the vertical velocity; $\mathbf{f}$, the vertical Coriolis vector; g, the gravitational acceleration; ζ, the surface displacement; ρ_0, a constant reference density; $\rho(\mathbf{x},z,t)$, the departure of the total density from ρ_0; and p is the baroclinic pressure divided by ρ_0. Further, α and v are the horizontal and vertical viscosity coefficients; α_t and v_t, the horizontal and vertical diffusion coefficients; and T and S are the fields of temperature and salinity. Finally, ∇ stands for the two-dimensional horizontal gradient operator, and D/Dt is the material derivative following a fluid particle,

$$\frac{D}{Dt} = \frac{\partial}{\partial t} + \mathbf{u} \cdot \nabla + w\frac{\partial}{\partial z}. \tag{6}$$

The velocity boundary conditions at the top and bottom surfaces are the kinematic boundary conditions of no-normal flow:

$$\frac{\partial \zeta}{\partial t} + \mathbf{u} \cdot \nabla\zeta = w \quad \text{on } z = \zeta, \tag{7}$$

$$\mathbf{u} \cdot \nabla h = -w \quad \text{on } z = -h, \tag{8}$$

and the dynamic boundary conditions specifying the stresses:

$$\left(\alpha\nabla\mathbf{u}^{\mathrm{T}} + v\frac{\partial \mathbf{u}^{\mathrm{T}}}{\partial z}\mathbf{k}\right) \cdot \mathbf{n} = \frac{\boldsymbol{\tau}}{\rho_0} \quad \text{on } z = \zeta, \tag{9}$$

$$\left(\alpha\nabla\mathbf{u}^{\mathrm{T}} + v\frac{\partial \mathbf{u}^{\mathrm{T}}}{\partial z}\mathbf{k}\right) \cdot \mathbf{n} = -\gamma\|\mathbf{u}\|\mathbf{u} \quad \text{on } z = -h, \tag{10}$$

where $\boldsymbol{\tau}$ is the prescribed wind-stress, $\mathbf{n}$ is the outward unit normal, $h(\mathbf{x})$ is the resting depth, γ is the quadratic drag coefficient, and $\mathbf{u}^{\mathrm{T}}$ refer to the transpose of $\mathbf{u}$.

On the lateral boundaries, we apply either a no-slip boundary condition: $\mathbf{u} = 0$, or free-stress boundary conditions: $\mathbf{u} \cdot \mathbf{n} = \nabla(\mathbf{u} \cdot \mathbf{t}) \cdot \mathbf{n} = 0$, where $\mathbf{t}$ is the tangent to the boundary in the horizontal direction. Notice that no boundary conditions are needed for w on the lateral surfaces of the domain since w is computed diagnostically from the continuity equation.

The boundary conditions for the tracers are of Neumann type

$$\left(\alpha_t\nabla T + v_t\frac{\partial T}{\partial z}\mathbf{k}\right) \cdot \mathbf{n} = Q, \tag{11}$$

$$\left(\alpha_t\nabla S + v_t\frac{\partial S}{\partial z}\mathbf{k}\right) \cdot \mathbf{n} = B, \tag{12}$$

where Q and B are the specified fluxes of heat and salinity, respectively.

The presence of the free surface gives rise to surface gravity waves that travel at speeds much larger than those of other phenomena of interest. The common cure, which we follow here, is to isolate the gravity waves in a set of two-dimensional equations which are integrated separately from those characterizing the three-dimensional circulation. The 2D equations are similar to the shallow water equations and can be obtained by vertical integration of the three-dimensional momentum and continuity equations:

$$\frac{\partial \zeta}{\partial t} + \nabla \cdot [(h + \zeta)\mathbf{U}] = 0, \tag{13}$$

$$\frac{\partial \mathbf{U}}{\partial t} + \mathbf{U} \cdot \nabla\mathbf{U} + \mathbf{f} \times \mathbf{U} + g\nabla\zeta = \frac{\boldsymbol{\tau}\sqrt{1 + |\nabla\zeta|^2}}{\rho_0(h + \zeta)} - \frac{\gamma[\|\mathbf{u}\|\mathbf{u}]_{z=-h}\sqrt{1 + |\nabla h|^2}}{h + \zeta} + \mathbf{D} - \mathbf{C}, \tag{14}$$

where **U** is the depth-average velocity

$$\mathbf{U} = \frac{1}{h+\zeta}\int_{-h}^{\zeta} \mathbf{u}\,\mathrm{d}z \tag{15}$$

and **D** represent the effect of the *horizontal* viscous dissipation on the depth-mean flow, and **C** is the coupling term between the two- and three-dimensional momentum equations. The derivation of the depth-averaged equations is outlined in Appendix A, and expressions for **C** and **D** are given in Eqs. (A.10) and (A.11). The first and second terms on the right-hand side of Eq. (A.10) contain the contributions of the baroclinic velocity and of the baroclinic pressure gradient to the depth-mean flow. The surface and bottom boundary conditions on the velocity have been used in the derivation of the depth-averaged equations.

3. Mapping of the free surface

Since the surface is moving, the domain V occupied by the fluid is time-dependent. In order to simplify the calculations, we map our domain to a steady computational space $(\mathbf{x}, Z, t)$ where

$$Z(\mathbf{x}, z, t) = h\frac{z-\zeta}{h+\zeta}. \tag{16}$$

The height $z \in [-h, \zeta]$ is thus mapped into the interval $Z \in [-h, 0]$.

Under this transformation, the horizontal gradient, material derivative, and divergence operators become

$$\nabla\Phi = \nabla_Z\Phi - \frac{\partial\Phi}{\partial Z}\frac{\partial Z}{\partial z}\nabla_Z z, \tag{17}$$

$$\frac{\partial\Phi}{\partial z} = \frac{\partial\Phi}{\partial Z}\frac{\partial Z}{\partial z}, \tag{18}$$

$$\frac{D\Phi}{Dt} = \left.\frac{\partial\Phi}{\partial t}\right|_Z + u\left.\frac{\partial\Phi}{\partial x}\right|_Z + v\left.\frac{\partial\Phi}{\partial y}\right|_Z + W\frac{\partial\Phi}{\partial Z}, \tag{19}$$

$$\nabla\cdot\mathbf{u} + \frac{\partial w}{\partial z} = \nabla_Z\cdot\mathbf{u} + \frac{\partial W}{\partial Z} + \frac{\partial Z}{\partial z}\frac{D}{Dt}\left(\frac{\partial z}{\partial Z}\right), \tag{20}$$

where $(\partial/\partial x)|_Z$, $(\partial/\partial y)|_Z$, and ∇_Z denote the x and y derivatives, and the horizontal gradient operator along constant Z-lines. W is the vertical velocity in the mapped space

$$W = \frac{DZ}{Dt} = \frac{\partial Z}{\partial z}\left(w - u\left.\frac{\partial z}{\partial x}\right|_Z - v\left.\frac{\partial z}{\partial y}\right|_Z - \left.\frac{\partial z}{\partial t}\right|_Z\right). \tag{21}$$

We note the following:

1. The solution of the equations in $(\mathbf{x}, Z, t)$ space requires that the above definitions of the gradient, divergence, material derivative, and vertical velocity be used for the discretization.
2. If Φ in Eq. (17) is depth-independent, then $\nabla\Phi = \nabla_Z\Phi$.
3. The evaluation of the integrals in the variational form (see below) require the integration over the volume of elements, and the latter involves the Jacobian of the mapping between the unsteady physical domain and the steady computational domain

$$J_s = \frac{\partial z}{\partial Z} = 1 + \frac{\zeta}{h} \approx 1 + \mathrm{O}\left(\frac{\zeta}{h}\right), \tag{22}$$

J_s is approximately equal to one since $\zeta \ll h$ except for the inner continental shelves and estuaries. This approximation amounts to neglecting variations in the volume of fluid due to the surface displacement. Computationally, it results in a tremendous savings in computational effort since the three-dimensional mass matrix becomes steady in time and need not be updated. This mapping has the additional benefit of preserving the structure of the three-dimensional equations provided the advection terms are evaluated with the new vertical velocity W.

4. Variational formulation

The variational formulation of Eq. (1) is:

$$\int_V \Phi\left[\frac{D\mathbf{u}}{Dt} + \mathbf{f}\times\mathbf{u} + g\nabla\zeta + \nabla p\right]\mathrm{d}V = -\int_V\left[\alpha\nabla\mathbf{u}^{\mathrm{T}}\cdot\nabla\Phi + \nu\frac{\partial\mathbf{u}^{\mathrm{T}}}{\partial z}\frac{\partial\Phi}{\partial z}\right]\mathrm{d}V + \int_{\partial V_{\mathrm{f}}}\frac{\boldsymbol{\tau}}{\rho_0}\Phi\,\mathrm{d}S - \int_{\partial V_{\mathrm{b}}}\gamma\|\mathbf{u}\|\mathbf{u}\Phi\,\mathrm{d}S, \tag{23}$$

where Φ is the three-dimensional test function associated with the velocity and tracer fields. ∂V_{f} refers to the free surface boundary, and ∂V_{b} refers to the sea-bed boundary. The boundary integrals weakly enforce the Neumann and Robin (mixed) boundary conditions imposed on the velocity field. Dirichlet boundary conditions are enforced by setting the test function Φ to zero on the Dirichlet portions of the boundary, and setting **u** equal to the imposed boundary value, e.g., zero on no-slip walls.

Likewise, the variational formulation of Eq. (4) is given by:

$$\int_V \Phi\frac{D}{Dt}\begin{pmatrix}T\\S\end{pmatrix}\mathrm{d}V = -\int_V\left[\alpha_t\nabla\begin{pmatrix}T\\S\end{pmatrix}\cdot\nabla\Phi + \nu_t\frac{\partial}{\partial z}\begin{pmatrix}T\\S\end{pmatrix}\frac{\partial\Phi}{\partial z}\right]\mathrm{d}V + \int_{\partial V}\begin{pmatrix}Q\\B\end{pmatrix}\Phi\,\mathrm{d}S. \tag{24}$$

The continuity equation is differentiated in the vertical before integration in order to ease the imposition of surface and bottom boundary conditions. Its variational formulation becomes:

$$\int_V \frac{\partial\Phi}{\partial z}\frac{\partial W}{\partial z}\mathrm{d}V = \int_V \frac{\partial\Phi}{\partial z}\frac{\partial Z}{\partial z}\left(\mathbf{U}\cdot\frac{\nabla h}{h} - \frac{\partial Z}{\partial z}\nabla_Z\cdot\left[\frac{\partial z}{\partial Z}(\mathbf{u}-\mathbf{U})\right]\right)\mathrm{d}V. \tag{25}$$

The variational formulation of the barotropic equations is a little more elaborate since the ζ field uses a staggered grid with respect to the velocity

$$\int_A \psi\frac{\partial\zeta}{\partial t}\mathrm{d}A - \int_A (h+\zeta)\mathbf{U}\cdot\nabla\psi\,\mathrm{d}A = \int_{\partial A}\psi q\,\mathrm{d}l, \tag{26}$$

$$\int_A \phi\left[\frac{\partial\mathbf{U}}{\partial t} + \mathbf{U}\cdot\nabla\mathbf{U} + \mathbf{f}\times\mathbf{U} + g\nabla\zeta\right]\mathrm{d}A = -\int_A \phi\frac{\gamma[\|\mathbf{u}\|\mathbf{u}]_{-h}\sqrt{1+|\nabla h|^2}}{h+\zeta}\mathrm{d}A + \int_A \phi\frac{\boldsymbol{\tau}\sqrt{1+|\nabla\zeta|^2}}{\rho_0(h+\zeta)}\mathrm{d}A + \int_A \phi[\mathbf{D}-\mathbf{C}]\,\mathrm{d}A, \tag{27}$$

where ψ and ϕ refer to the two-dimensional test functions associated with ζ and **U**, respectively. The divergence term in the continuity equation has been integrated by parts to allow the imposition of inflow as weak boundary conditions, and to produce a symmetric positive matrix equation for ζ in case an implicit integration scheme is adopted (see Section 6). The q in (26) refers to the inflow per unit width. Notice that the integrals in the above equations are performed over a horizontal surface.

5. Spatial discretization

The spatial discretization relies on isoparametric and conforming hexahedral elements (cubes with curved surfaces) with C^0 continuity. The three-dimensional variables in each element are approximated with a high-order Lagrangian interpolant whose collocation points are the Gauss–Lobatto roots of the Legendre polynomials. Hence, the 3D fields in element e are interpolated as:

$$\begin{pmatrix} \mathbf{u}(\xi,\eta,\sigma) \\ w(\xi,\eta,\sigma) \\ T(\xi,\eta,\sigma) \\ S(\xi,\eta,\sigma) \\ \rho(\xi,\eta,\sigma) \\ p(\xi,\eta,\sigma) \end{pmatrix} = \sum_{l=1}^{N}\sum_{m=1}^{N}\sum_{n=1}^{M} \varphi_l^v(\xi)\varphi_m^v(\eta)\chi_n^v(\sigma) \begin{pmatrix} \mathbf{u}_{lmn}^e \\ w_{lmn}^e \\ T_{lmn}^e \\ S_{lmn}^e \\ \rho_{lmn}^e \\ p_{lmn}^e \end{pmatrix}, \tag{28}$$

where φ_i^v and φ_j^v are the horizontal interpolation functions, χ_k^v is the vertical interpolation function, (ξ,η,σ) is the local coordinate system in element e, N is the number of collocation points in each horizontal direction, M is the number of collocation points in the vertical, and $\mathbf{u}_{lmn}^e$ is the value of $\mathbf{u}$ at the (N,N,M) Gauss–Lobatto–Legendre roots $(\xi_l^v,\eta_m^v,\sigma_n^v)$; for details see [1,10]. Notice that we have kept the order of the interpolation in the vertical and horizontal directions separate since the vertical and horizontal structures of the solution may be quite different. It is best to keep the orders of the vertical and horizontal interpolations independent so they can be adjusted individually to achieve the best *h–p* balance in each direction.

The two-dimensional variables are interpolated according to

$$\mathbf{U}(\xi,\eta) = \sum_{l=1}^{N}\sum_{m=1}^{N} \varphi_l^v(\xi)\varphi_m^v(\eta)\mathbf{U}_{lm}^e, \tag{29}$$

$$\zeta(\xi,\eta) = \sum_{l=1}^{N-2}\sum_{m=1}^{N-2} \varphi_l^p(\xi)\varphi_m^p(\eta)\zeta_{lm}^e, \tag{30}$$

where φ_l^p refers to the surface displacement interpolation function whose collocation points are given by the $(N-2)$ Gauss–Lobatto–Legendre roots. The ζ collocation points are staggered with respect to those of $\mathbf{U}$ in order to eliminate spurious pressure oscillations when the barotropic flow is almost divergence-free (see [10]).

Given the complicated bathymetry of ocean basins, and the lack of appropriate three-dimensional grid generation software, we have decided to simplify the elemental partitioning in the vertical by restricting it to a structured discretization, i.e., the number of vertical elements does not vary horizontally. A three-dimensional spectral element grid can thus be produced by stacking vertically and conformally a number of two-dimensional grids. In addition, we require that the local coordinate lines be vertical in order to decouple the vertical and horizontal calculations. This decoupling reduces the operation count tremendously if, for example, vertical diffusion is integrated implicitly. These two restrictions are not severe since we are still able to fit the three-dimensional elements to the bathymetry of the basin, to distribute vertical resolution according to a priori considerations, and to retain the unstructured nature of the grid in the horizontal direction. A vertical slice of a sample spectral element grid is shown in Fig. 2.

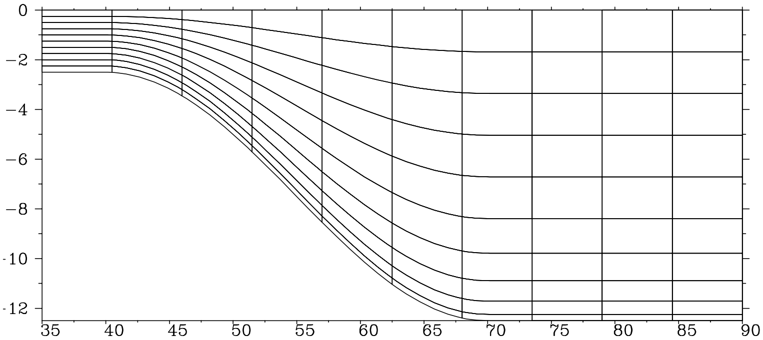

Fig. 2. Vertical slice of a 3D spectral element grid used in the canyon simulations showing the elemental partition. The elements are refined near the bottom to improve the resolution of near-bed dynamics. The vertical and horizontal scales are in centimeters.

The interpolations (28) and (30) are substituted into the Galerkin formulation to yield a system of ordinary differential equations, after setting

$$\Phi = \varphi_i^v(\xi)\varphi_j^v(\eta)\chi_k^v(\sigma), \tag{31}$$

$$\phi = \varphi_i^v(\xi)\varphi_j^v(\eta), \tag{32}$$

$$\psi = \varphi_i^p(\xi)\varphi_j^p(\eta), \tag{33}$$

and evaluating the resulting integrals numerically.

6. Temporal discretization

Eqs. (1)–(5), (13) and (14) form a tightly coupled system of nonlinear partial differential equations that must be integrated in time. The prognostic variables are the horizontal velocity **u**, the temperature T, the salinity S, the surface displacement ζ, and the barotropic velocity **U**. The vertical velocity, density, and baroclinic pressure are calculated diagnostically from the continuity equation, the equation of state, and the hydrostatic equation, respectively.

The temporal discretization of Eq. (1) is based on a semi-implicit integration scheme. The non-linear advection term, the Coriolis term, the horizontal viscous term, and the baroclinic pressure gradient term are integrated with a third-order Adams–Bashforth (AB3) time step. The vertical viscous term is integrated with an implicit second-order Crank–Nicholson scheme for enhanced numerical stability, since the vertical viscosity v may need to be increased during calculations to simulate rapid vertical mixing associated with convective overturning events. Finally, the barotropic pressure gradient is integrated with a fully implicit backward Euler scheme to damp the high-frequency waves effectively.

The time-discretized momentum equations have the form

$$\left[\frac{M}{\Delta t} + \theta D^z\right] u^{t+1} = a^x - gG^x\zeta^{t+1}, \tag{34}$$

$$\left[\frac{M}{\Delta t} + \theta D^z\right] v^{t+1} = a^y - gG^y\zeta^{t+1}, \tag{35}$$

where M is the diagonal three-dimensional mass matrix, the matrix D^z is the discrete vertical Laplace operator, θ is the weight factor of the implicit scheme ($\theta = \frac{1}{2}$ for the Crank–Nicholson scheme), G^x and G^y are the gradient operators in the x and y directions, and a^x and a^y contain the explicitly treated terms and the terms known from previous time levels in the horizontal momentum equations. We have shown ζ^{t+1} on the right-hand sides to emphasize that the surface displacement is computed from the barotropic equations, and appears as a forcing term in the three-dimensional equations. Note that the mass matrix is diagonal because the integrals in the variational formulations are evaluated with Gauss–Lobatto–Legendre quadrature and the weight functions are the Legendre cardinal functions [1].

The tracer equations are also integrated in time with a semi-implicit scheme: AB3 for the advection and horizontal diffusion terms and second-order Crank–Nicholson for the vertical diffusion term. In matrix notation, the tracer equations become:

$$\left[\frac{M}{\Delta t} + \theta D^z\right]\begin{pmatrix} T \\ S \end{pmatrix}^{t+1} = \begin{pmatrix} f^T \\ f^S \end{pmatrix}. \tag{36}$$

Our current code supports two methods of integration for the barotropic Eqs. (13) and (14): a semi-implicit scheme and a split-explicit scheme. In the semi-implicit scheme, all terms are treated explicitly with AB3 except for the pressure gradient term, $\nabla\zeta$, in Eq. (14) and the linear divergence term, $\nabla \cdot (h\mathbf{u})$, in Eq. (13) which are integrated with a backward Euler scheme. These two terms are responsible for the existence of the fast gravity waves and their implicit treatment eliminates the severe explicit time step restriction. The matrix form of the barotropic equations is thus:

$$\frac{M^v}{\Delta t} U^{t+1} + \mathscr{G}^x \zeta^{t+1} = b^x, \tag{37}$$

$$\frac{M^v}{\Delta t} V^{t+1} + \mathscr{G}^y \zeta^{t+1} = b^y, \tag{38}$$

$$\frac{M^p}{\Delta t} \zeta^{t+1} - \mathscr{K}^x U^{t+1} - \mathscr{K}^y V^{t+1} = c. \tag{39}$$

Eqs. (37)–(39) can be integrated with a large time step whose size is dictated by the time scales, or stability restrictions, of baroclinic dynamics. The advantage of this approach is that the barotropic equations can be integrated synchronously with the three-dimensional equations. Its disadvantage is mainly computational: a system of simultaneous algebraic equations must be solved at each time step. Since the system is symmetric positive definite, we solve the equations with conjugate gradient iterations.

The split-explicit scheme introduces a two-time-step integration process. First the barotropic equations are integrated explicitly using a small time step, Δs, that respects the CFL stability limit of the gravity waves. The barotropic equations take the form:

$$\frac{M^v}{\Delta s} U^{t,s+1} = \hat{b}^x, \tag{40}$$

$$\frac{M^v}{\Delta s} V^{t,s+1} = \hat{b}^y, \tag{41}$$

$$\frac{M^p}{\Delta s} \zeta^{t,s+1} = \hat{c}. \tag{42}$$

If the ratio between the long and short time step is denoted by L, then the above integration is carried out from $s = 0$ to $s = 2L$. The surface displacement thus calculated is time-averaged to filter out the fast time scales and

$$\begin{pmatrix} \mathbf{U}^{t+1} \\ \zeta^{t+1} \end{pmatrix} = \frac{1}{2L+1} \sum_{s=0}^{2L} \begin{pmatrix} \mathbf{U}^{t,s} \\ \zeta^{t,s} \end{pmatrix}. \tag{43}$$

The time-average is also necessary to eliminate incipient instabilities [9]. The three-dimensional equations are then integrated, using the filtered surface displacement, on a long time step whose size can be chosen based on the time scales of the baroclinic dynamics. The main advantage of this procedure is that it avoids the solutions of a system of equations, and is simple to implement. Its main disadvantage is that it complicates the evaluation of the coupling term, **C**, between the barotropic and three-dimensional equations. In our current implementation, this term is fixed in time at the previous time level and is updated only after the integration of the three-dimensional equations. Moreover, the time-filtering exacts a computational penalty: in order to center the time-averaging procedure around the next long time level, $(t+1)\Delta t$, the barotropic equations must be integrated until time level $(t+2)\Delta t$ before the averaging procedure is applied. We have used the split-explicit scheme in all the computations presented herein.

7. Solution procedure

The solution proceeds as follows:

1. The two-dimensional equations are integrated to calculate the surface displacement at the new time level, ζ^{n+1}, and the depth-averaged velocity, $\mathbf{U}^{n+1}$. This step requires the solution of a two-dimensional system of equations if the semi-implicit scheme is used.
2. ζ^{n+1} is substituted into the three-dimensional momentum equations to update the three-dimensional horizontal velocity, $\mathbf{u}^{n+1}$. This calculation is explicit unless implicit treatment of vertical mixing is applied. At the end of this second step, two estimates for the depth-averaged velocity are available: one from the integration of the 2D equations and another from the 3D equations

   $$\tilde{\mathbf{U}} = \frac{1}{h+\zeta^{n+1}} \int_{-h}^{\zeta^{n+1}} \mathbf{u}\,\mathrm{d}z. \tag{44}$$

   This artifact is a result of the separate integration of the slow and fast waves. A correction term, $(\mathbf{U}^{n+1} - \tilde{\mathbf{U}})$, is added to $\mathbf{u}^{n+1}$ in order to prevent a slow drift of the two estimates, and to ensure that the depth-averaged components are integrated with a small time step.
3. The tracer equations are integrated in time to calculate the new temperature and salinity fields. This phase of the update is also explicit unless a convective parameterization is used to mix the tracers vertically when the water column becomes statically unstable.
4. The horizontal divergence of $\mathbf{u}^{n+1}$ is evaluated and integrated vertically to calculate the vertical velocity W^{n+1}.
5. The equation of state is used to compute the density field ρ^{n+1} implied by the new temperature and salinity. The baroclinic pressure gradient is then updated with the help of Eq. (53), see Section 8.

The majority of the computations are associated with the calculation of the right-hand sides of the prognostic and diagnostic equations. These calculations can be effectively carried out at the element level by first computing the local effect of the operators in each element before assembling the elemental vectors. The assembly procedure affects nodes that are shared by more than one element and the resultant communication pattern is solely neighbor-to-neighbor. The local computations consist mostly of the calculation of the gradients of various fields and of integrals arising from the Galerkin formulation. The efficiency of these computations is enhanced by the tensor product nature of the basis functions which allows a compact summation scheme to be implemented in each direction. Furthermore, the implementation of explicit integration is straightforward since all the mass matrices are diagonal; hence, they require little storage and their inverse is trivial to calculate.

The system of equations generated by the semi-implicit integration of the barotropic equations is solved using conjugate gradient (CG) iterations. Iterative solutions are indispensable to reduce the memory and cpu costs associated with the solution of the very large system of equations which results from the implicit treatment. The conjugate gradient method has the additional benefits of dispensing with the assembly of a large system of equations, preserving the locality of the computations at the element level, and scalability and ease of implementation on parallel computers. The CG method preserves the assembly pattern of an explicit integration scheme since the effect of the operators can be calculated in each element before assembling the resultant vectors of residuals. The only global operations necessary in CG are the inner-product and residual calculations which require the broadcast of scalars.

The systems of equations generated by a potential implicit integration of the vertical diffusion and/or viscous terms during the second and third phase of the calculations would also be solved with conjugate gradient iterations. Note that, although these equations originate from three-dimensional partial differential equations, they couple only the nodes aligned along the vertical direction – a consequence of restricting the coordinate lines in the reference element to be strictly parallel to the vertical direction. The system thus consists of a large number of horizontally uncoupled, vertically coupled small systems of equations. We have opted to avoid solving these small systems with a direct method since their bandwidth is larger than three, thus precluding tri-diagonal solvers, and the viscosity and diffusion coefficients are time-dependent and would thus require multiple re-assembly and re-factorization steps.

The calculation of the vertical velocity generates a system of equations similar in structure to the ones produced by the vertical diffusion terms. We solve this system by applying a direct method to the vertically coupled equations. We reiterate that the continuity equation is differentiated first in the vertical to enforce strongly and simultaneously the surface and bottom Dirichlet conditions on W. In its original form, the continuity equations affords only one boundary conditions, and the other condition is met only “weakly” in the sense that the errors incurred decrease as the exact solution is approached. The differentiation device used here avoids the numerical drift of the vertical velocity at the surface or bottom, and can be shown to be equivalent to a least-square enforcement of the continuity equation.

The computation of the density field from salinity and temperature information, whether from a linear or nonlinear equation of state, involves polynomial evaluations only; no system of equations needs to be solved. We now turn to the issue of computing ∇p.

8. Baroclinic pressure gradient

Care must be taken when computing the horizontal baroclinic pressure gradient since this term is among the most significant in the momentum equations. The traditional procedure for this calculation is to integrate the hydrostatic equation for the pressure before differentiating it:

$$b = \frac{g\rho}{\rho_0}, \quad p = \int_z^{\zeta} b(\mathbf{x}, z', t)\,\mathrm{d}z', \quad \nabla p = \nabla_Z p + b\nabla_Z z. \tag{45}$$

It is well known that terrain-following methods like the present one suffer from pressure gradient errors in the presence of topography and stratification. We proceed to quantify these errors by focussing on a simple configuration: a two-dimensional vertical slice across a shelf like coastline as shown in Fig. 3 where, the

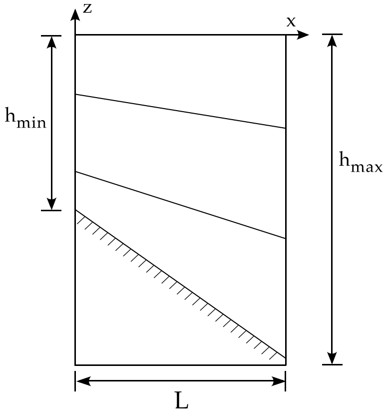

Fig. 3. Sketch of a shelf like coastline discretized with three spectral elements in the vertical using a sigma-like partition.

(ξ,η) computational lines are aligned along the cross-shelf (x) and along shelf (y) directions, respectively. In what follows we neglect the motion of the free surface, and assume that properties are homogeneous in the along-shelf direction for the sake of simplicity. The cross-shelf baroclinic pressure gradient in the offshore direction is computed with the help of the chain rule of differentiation:

$$p_x = p_\xi \xi_x + p_\sigma \sigma_x, \tag{46}$$

where the terms ξ_x and σ_x are the metrics of the mapping of the 3D spectral element into computational space. Let

$$\overline{p}_x = \overline{p}_\xi \overline{\xi}_x + \overline{p}_\sigma \overline{\sigma}_x \tag{47}$$

be the approximated pressure gradient (all variables with an overline will refer to numerical approximations). The difference between expressions (46) and (47) define the error

$$E = \overline{p}_x - p_x \tag{48}$$

$$= \overline{p}_\xi(\overline{\xi}_x - \xi_x) + \xi_x(\overline{p}_\xi - p_\xi) + \overline{p}_\sigma(\overline{\sigma}_x - \sigma_x) + \sigma_x(\overline{p}_\sigma - p_\sigma). \tag{49}$$

The hydrostatic approximation can be invoked to show explicitly the dependency of the hydrostatic error on the density. This is straightforward for the last component of the error since $p_\sigma = -bz_\sigma$, hence:

$$\overline{p}_\sigma - p_\sigma = -z_\sigma(\overline{b} - b) - b(\overline{z}_\sigma - z_\sigma), \tag{50}$$

where z_σ is the stretching factor in the vertical. The expression for the second component is more complicated since it involves the integration of the interpolated density field prior to differentiation. The error in calculating the pressure field itself can be expressed as

$$\overline{p} - p = \left(\overline{\int_z^0 (\overline{b} - b)\,\mathrm{d}z}\right) + \left(\overline{\int_z^0 b\,\mathrm{d}z} - \int_z^0 b\,\mathrm{d}z\right). \tag{51}$$

The overline over the sign integral refer to the fact that the integral is evaluated with Gauss quadrature. The first term on the right-hand side of (51) represents the error committed in interpolating the buyoancy, while the second term is the error in approximating the integral by Gaussian quadrature. This second component is small because of the high-order quadrature used: an M point Gauss–Lobatto quadrature in the vertical integrates exactly a polynomial of degree less or equal to $2M - 3$. Eqs. (49)–(51) shows that there are several factors contributing to the pressure gradient error: approximations of the metric factors ξ_x, σ_x, approximations of the density fields and its (vertical) integration with Gauss quadrature, and finally errors in interpolating and differentiating the hydrostatic pressure (the second term in (49)). In Appendix A we derive a bound on the errors incurred by the representation of the geometry of Fig. 3.

An alternative form to the baroclinic pressure gradient has been proposed in recent years [18], and consists of interchanging the order of integration and differentiation in Eq. (45):

$$\nabla p = \int_z^\zeta \nabla b \, \mathrm{d}z + b|_\zeta \nabla \zeta \tag{52}$$

$$= \int_Z^0 (z_Z \nabla_Z b - b_Z \nabla_Z z) \, \mathrm{d}Z' + b|_\zeta \nabla \zeta. \tag{53}$$

The prime virtues of the above form is that it dispenses with the interpolation of the pressure field as an intermediate variable (Song [18] has investigated the properties of the above formulation for finite difference models). Like the traditional scheme, the errors associated with (53) depend on geometric errors, on the quality of the integration, and on the interpolation and differentiation of the density field. We have implemented both schemes to compute ∇p in our model, and we have found that the error incurred is similar in both forms.

9. Model performance: Kelvin waves

The favorable convergence properties of the method described here may be verified by reference to an analytical solution describing the propagation of a baroclinic Kelvin wave in a periodic channel of constant depth h and width b. The linearized equations that include the motion of the free surface are:

$$u_t - fv = -p_x - g\zeta_x, \tag{54}$$

$$v_t + fu = -p_y - g\zeta_y, \tag{55}$$

$$p_z = -g\frac{\rho'}{\rho_0}, \tag{56}$$

$$u_x + v_y + w_z = 0, \tag{57}$$

$$\rho_t + w\overline{\rho}_z = 0. \tag{58}$$

Here we have split the perturbation density into two parts: $\rho = \overline{\rho}(z) + \rho'$ and we have assumed $\rho' \ll \overline{\rho}$. In addition to periodicity in time and in the long channel direction (x), we impose the boundary conditions $\zeta_t = w$ and $p = 0$ on $z = 0$, $w = 0$ on $z = -h$, and $v = 0$ on $y = 0, b$.

For cases where the Coriolis parameter is constant and the stratification is linear, the Kelvin wave solutions are:

$$u = \frac{kga}{\sigma \cos \beta h} \cos \beta(z + h) \, \mathrm{e}^{-\mu y} \cos(kx - \sigma t), \tag{59}$$

$$v = 0, \tag{60}$$

$$w = \frac{kga}{N\cos\beta h}\sin\beta(z+h)\,\mathrm{e}^{-\mu y}\sin(kx-\sigma t), \tag{61}$$

$$\rho' = \frac{\rho_0\beta a}{\cos\beta h}\sin\beta(z+h)\,\mathrm{e}^{-\mu y}\cos(kx-\sigma t), \tag{62}$$

$$p = \frac{\rho_0 g a}{\cos\beta h}[\cos\beta(z+h) - \cos\beta h]\,\mathrm{e}^{-\mu y}\cos(kx-\sigma t), \tag{63}$$

$$\zeta = a\,\mathrm{e}^{-\mu y}\cos(kx-\sigma t). \tag{64}$$

Here, a is the (arbitrary) amplitude of the surface displacement, N is the buoyancy frequency ($N^2 = -g\overline{\rho}_z/\rho_0$), $\sigma = kN/\beta$ is the frequency of the motion, $\mu = \beta f/N$ is the off-shore decay scale, and β are the solutions to the dispersion relation:

$$\beta\tan\beta h = \frac{N^2}{g}. \tag{65}$$

The emphasis in this section is on the convergence behavior of the model as the horizontal resolution is varied. For this reason we use a fixed high-order representation in the vertical, 4 elements of spectral truncation of 9, to minimize the effects of vertical truncation errors. The model was initialized from the analytical solution using the following parameters: $f = 10^{-4}$ s^{-1}, $h = 1000$ m, $g = 9.81$ m/s^2, $N = 20\pi f$, $k = 2\pi/200$ km^{-1}, and a pressure amplitude $a/\cos\beta h = 1$ m. The equations were integrated for a single wave period using a time step small enough that the error is dominated by spatial truncation errors. The resulting convergence curves are plotted in Fig. 4 and show the difference between the numerical and analytical solutions as a function of horizontal resolution. As expected the error decreases at an algebraic rate that depends on the spectral truncation for h-refinement. The convergence is exponential under p-refinement as is evident in the bottom right panel of Fig. 4.

10. Gravitational adjustment

We investigate the ability of the spectral element model to track the propagation of a density front in a channel of uniform cross-section. The problem involves the gravitational adjustment of a two-density-layer system, initially separated by a vertical wall [24]. The system is illustrated in Fig. 5. At time zero, the vertical wall dividing the two immiscible fluids is removed; thereafter, the fluid layers adjust at the internal gravity-wave phase speed to form a stably stratified, two-layer system. During and after the adjustment, sharp density fronts divide the two layers both horizontally and vertically.

The gravitational adjustment problem is difficult because it tests the ability of the numerical model to propagate a narrow moving front. Diffusive and dispersive errors stemming from the discretization can destroy the structure of the solution quickly. The trouble manifests itself in the form of oscillations in the density field, unphysical density extrema in the neighborhood of the front, and a distorted phase speed. A faithful model would thus eliminate the oscillations, maintain the extrema of the density fields at their initial values, and produce as narrow a front as possible while propagating it at the correct phase speed.

High-order methods are at a particular disadvantage in this class of problems because the front discontinuity defeats the spectral convergence of the method. The remedy we use here is to employ a small but finite amount of diffusion to suppress the oscillations; the width of the front is thus numerically increased until it is resolvable on the computational grid. Fig. 6 shows the density structure after 10 h of simulated time for two values of the dissipation and diffusion parameters. A reference solution obtained with

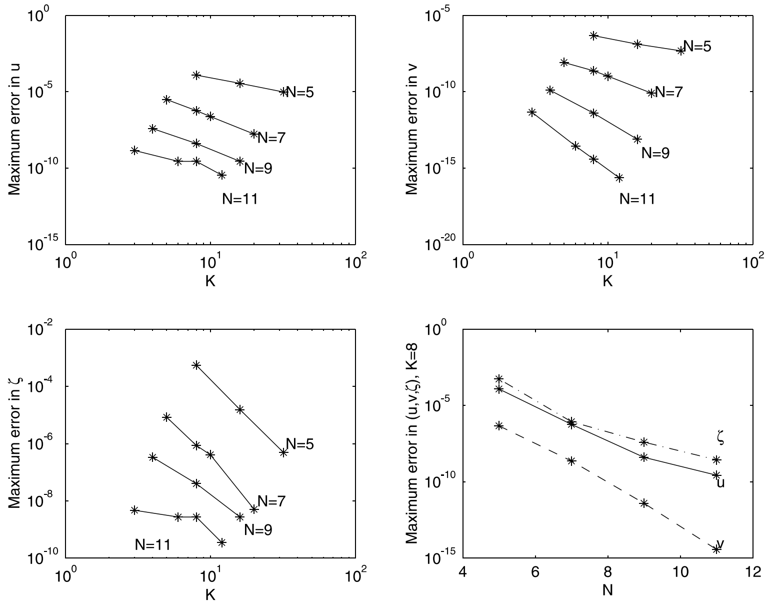

Fig. 4. Convergence curves for the baroclinic Kelvin wave problem. K refers to the number of elements in the periodic direction and N to the spectral truncation in the horizontal. The two top panels and the bottom left panels show the reduction in error as K increases for fixed N (h-refinement). The bottom right panel shows the exponential decrease of the error as N increases, for a fixed elemental partition, $K = 8$ (p-refinement).

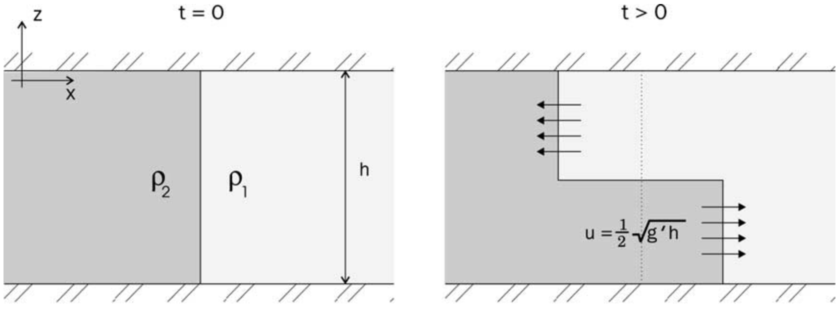

Fig. 5. Sketch of the gravitational adjustment test problem The model domain is 64 km long and 20 m deep, and spatial resolution is fixed at 0.5 km in the horizontal and 1 m in the vertical. The initial density contrast across the vertical front is 5 kg/m^3; here $\rho_2 > \rho_1$.

SCRUM [19], a finite-difference based ocean model with a second-order centered advection scheme, is included for comparison. Table 1 lists the values of the density extrema and the phase speeds obtained with the two models.

The high-order spectral element solutions are quite similar in propagation speed and smoothness to the results obtained with centered differences. Both models require sufficient explicit viscosity and diffusivity (in the range 50–100 m^2/s) to produce smooth well-behaved solutions. The two exhibit the same behavior in that the amplitude of the oscillations grows with decreasing dissipation parameters; however, the estimate of the phase speed is improved for the spectral element solution over the centered-difference results as shown in Table 1. In this instance, the high-order method produces smaller spurious extrema than does the low-order model with centered differencing. This test shows that once a level of “adequate” resolution is

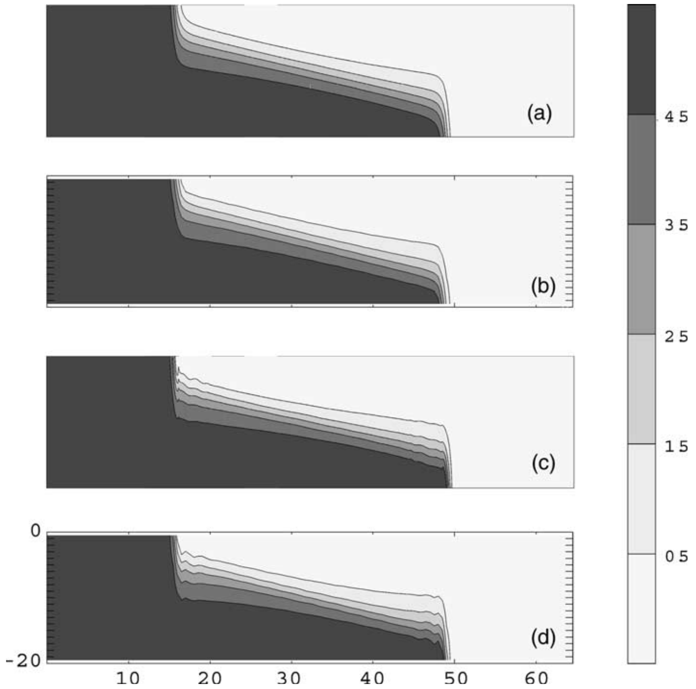

Fig. 6. Comparison of results from spectral element model and SCRUM for the gravitational adjustment test problem: (a) spectral element model, $\nu = \alpha = 100\ \mathrm{m}^2\,\mathrm{s}^{-1}$; (b) SCRUM, $\nu = \alpha = 100\ \mathrm{m}^2\,\mathrm{s}^{-1}$; (c) spectral element model, $\nu = \alpha = 50\ \mathrm{m}^2\,\mathrm{s}^{-1}$; and (d) SCRUM, $\nu = \alpha = 50\ \mathrm{m}^2\,\mathrm{s}^{-1}$. The contour interval is 0.5 kg/m^3 starting at 0.5 kg/m^3.

Table 1
Minima, maxima, and phase velocity relative to the analytical solution for the gravitational adjustment experiment after 10 h of integration

Model	Diffusion	Viscosity	Min (ρ)	Max (ρ)	Phase speed
SCRUM-centered	100	100	−0.156	5.138	0.913
SCRUM-centered	50	50	−1.678	6.603	0.927
Spectral element	100	100	−0.044	5.000	0.912
Spectral element	50	50	−0.540	5.601	0.932

The phase velocities are determined by computing the horizontal distance between the surface and bottom location of the 2.5 sigma-units density contour, divided by the time since the release of the front.

reached, the properties of the high-order solution (including over- and under-shooting) are better than those from low-order centered schemes. We refer the reader to [7] for further discussion of this, and other, idealized ocean model test problems.

11. Residual circulation at a coastal canyon

Ultimately, numerical ocean models must be validated against observed geophysical flows. Unfortunately, such comparisons are not easy to perform. The difficulties arise from the complexity of geophysical flows which encompass a wide variety of processes resulting from a subtle interplay between rotation, stratification, bathymetric variations, turbulent mixing, and other effects. Related to this is the difficulty of obtaining datasets of adequate accuracy and space/time coverage for model initialization, forcing, and validation.

Carefully designed laboratory experiments offer an important alternative for model verification by providing a controlled setting wherein some of the difficulties associated with obtaining data in the field can be avoided. In a recent example, Perenne et al. [17] have carried out a series of laboratory experiments to simulate the three-dimensional time-mean circulation near a submarine canyon. Their aim is to provide an independent reference "solution" which can be used to validate and improve the realism of ocean models. Initial numerical experiments, conducted with SEOM, are used as a first means of comparison.

The geometry of the laboratory and numerical experiments, shown in Fig. 7, is an annulus of 0.90 m radius. The bathymetry is an idealized continental shelf/slope interrupted by a single canyon. The laboratory forcing arises from a modulation in the background rotation rate. This is equivalent to a body force proportional to the distance *r* from the center of the turntable. In the rotating reference frame, the result of this body force is a depth-independent, oscillatory, along-coast current. In the absence of any azimuthal variations in topography, the imposed forcing will not generate any time-mean (residual) currents. In the

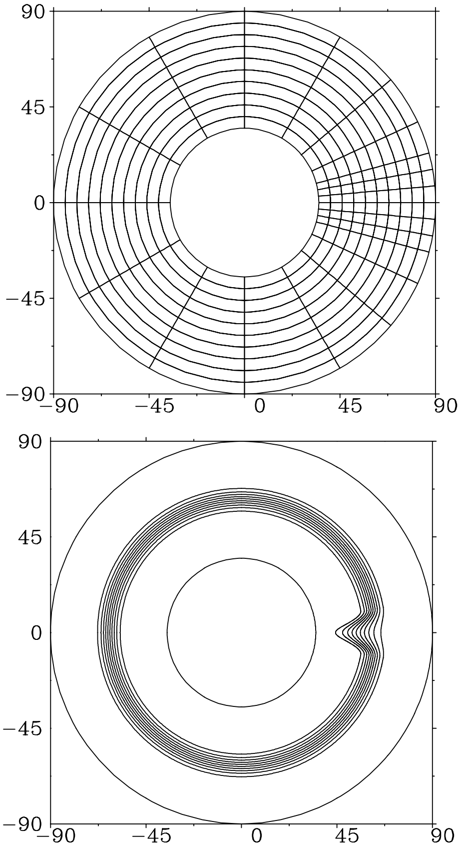

Fig. 7. The top panel shows the elemental discretization of the domain. In this case, the resolution is enhanced in the vicinity of the canyon. The inner cylinder representing the coast has a radius of 0.35 m and the outer cylinder has a radius of 0.90 m. The depth contours are shown in the bottom panel (contour interval 0.01 m). The shallow regions near the inner cylinder have a depth of 0.025 m and the "off-shore" depth near the outer cylinder is 0.125 m. The characteristic azimuthal and radial length scales of the canyon are 0.20 and 0.10 m, respectively.

presence of the coastal canyon, however, a significant residual circulation can arise. The structure and strength of this residual current is the basis for comparison between the laboratory measurements and the numerical simulations.

From a geophysical perspective, a matter of much interest is the net three-dimensional circulation associated with coastal canyons, especially any time-mean cross-shelf exchange of fluid. Such enhancements of cross-shelf exchange may have important consequences for biological productivity, carbon cycling, etc. We note finally that barotropic tidal forcing on continental shelves provides a close mechanical analogue of the oscillatory forcing which arises in these idealized experiments.

The environmental parameters which characterize this physical system include the height and width of the canyon, the background rotation rate (and the amplitude and frequency with which it is modulated), and the strength of the background stratification. Values of these environmental parameters were chosen so as to approximately replicate the expected oceanic values of the essential non-dimensional parameters (topographic aspect ratios, and the Rossby and Burger numbers). The latter two parameters express the non-dimensional magnitude of non-linearity and stratification, and have values in these experiments of 0.1 and 10.0, respectively. Perenne et al. [17] describe in detail the choice of environmental parameters, and their similarity to those encountered in the ocean.

The numerical solutions have been obtained using SEOM implemented in the annular geometry of Fig. 7. Additional terms have been added to the momentum equations in SEOM to incorporate the effects of the modulation in the background rotation rate introduced in the laboratory [17]. All of the macroscopic non-dimensional parameters in the numerical model are identical to those in the laboratory. The lowest achievable values of subgridscale viscosities and diffusivities are, however, greater than molecular values by factors of from 10 to 100. These minimum values depend greatly on such choices as vertical resolution and the bottom boundary conditions applied.

The three experiments we discuss here are summarized in Table 2. Experiment E1 was the central case described by Perenne et al. [17]. It has the lowest vertical resolution – eight, third-order elements (a total of 25 points) uniformly distributed in the vertical – and a minimum value of horizontal numerical viscosity of 10^{-4} m^2/s, which is larger than molecular viscosity by a factor of 100. In these earlier numerical simulations, the best results were obtained with a molecular value of vertical viscosity (10^{-6} m^2/s) and a linear bottom stress parameterization to represent the (laminar) bottom boundary layer thought to occur in the laboratory flow:

$$\boldsymbol{\tau} = -\rho_0\sqrt{\frac{\nu f}{2}}\mathbf{u}\big|_{z=-h} = -0.05\mathbf{u}\big|_{z=-h}. \tag{66}$$

The height of the Ekman boundary layer is $\delta_{\mathrm{E}} = \sqrt{2\nu/f}$ or about 2 mm for the physical flow.

With this choice of parameters, experiment E1 required a time step of 1 ms, as dictated by the viscous CFL condition arising from the value of the horizontal viscosity and the minimum *vertical* grid spacing. (Note: because the "horizontal" computational surfaces in SEOM are terrain-following, a truly geopotential viscosity will have projections both along the terrain-following surfaces and along the vertical. Since

Table 2
Viscous parameters, vertical gridding, and bottom boundary condition for the three canyon experiments

Experiment	Viscosity (horiz./vert.)	Diffusivity (horiz./vert.)	Vertical resolution	Vertical stretching	Bottom BC
E1	$10^{-4}/10^{-6}$	$10^{-5}/0$	8@4	Uniform	Stress-law
E2	$10^{-4}/10^{-6}$	$10^{-5}/0$	20@6	Uniform	No-slip
E3	$10^{-5}/10^{-5}$	$10^{-5}/0$	10@6	Stretched	No-slip

All units are mks.

the slopes here are O(1), the resulting projection of horizontal viscosity onto the vertical is of the same order as the horizontal viscosity itself. Since explicit time stepping is being used for these viscous terms, a very stringent CFL limit applies.)

Considerations which arise in the Perenne et al. comparisons, see below, have since led us to attempt to improve upon the viscous parameterizations in E1. Experiments E2 and E3 (Table 2) are two more recent simulations in which lower values of horizontal viscosity and/or a true no-slip bottom boundary condition have been employed. These improvements required more resolution in space and time, however. In our first no-slip experiment (E2), vertical resolution was incresed to 101 points (20, fifth-order elements), and the required time step decreased to 40 μs. A more economical, and less viscous, simulation (E3) is able to reduce the horizontal viscosity to within a factor of 10 of the molecular value, and to reduce the total number of points in the vertical to 51 (10, fifth-order elements) by using a stretched distribution of elements (Fig. 2). Because of the reduced horizontal viscosity in E3, the required time step could be increased to 400 μs.

Both the laboratory and numerical experiments were run for 10 forcing cycles to allow initial transients to disappear, then an average of the circulation over an additional two cycles was performed to obtain the residual circulation. The results shown below are all windowed on a small area surrounding the canyon.

Perenne et al. [17] discuss three levels of laboratory/numerical model comparison based upon horizontal velocity measurements. These three levels of comparison, which are in increasing level of stringency, are: comparison of the directly forced (time varying) flow, comparison of the residual (time-averaged) flow, and comparison of the residual horizontal vorticity and divergence fields. Comparisons of the first two of these were generally good in the Perenne et al. study. For example, Fig. 8 shows the residual flow at the shelf-break level in the laboratory model and in experiment E1. There is a good qualitative and quantitative agreement between the laboratory and numerical experiments. The order of magnitude of the residual currents is the same in both models; the anticyclonic loop at the upstream corner is more defined in the laboratory model but still identifiable in the numerical results, which also exhibits an intensification of the residual current at the upstream wall of the canyon although it is more distributed along the shelf-break. A residual current emanating from the canyon at its downstream corner is also present in the numerical solution. The main quantitative discrepancy between the laboratory and numerical results is that the numerical model generates a somewhat stronger residual circulation; this current is partly recirculating but is intensified in regions where it leaves the shallow water on its right. Note, lastly, that both models produce a weak influx to the canyon along its axis, suggestive of net cross-shelf exchange. We return to this issue below.

Despite these generally good comparisons of the residual horizontal currents, Perenne et al. found rather less good agreement in the residual vorticity and divergence fields. These higher-order dynamical quantities are of much interest – as they are indicative of the underlying patterns of three-dimensional circulation and the degree of nonlinearity of the residual currents. As a consequence, they represent a much more stringent test of model/model agreement. In the Perenne et al. study, the vorticity exhibits good structural agreement between the two models although the maximum vorticity appears to be somewhat weaker in the numerical model. In contrast, the numerical residual divergence field in experiment E1 is qualitatively different from that measured in the laboratory.

Since the spectral element algorithms used here are designed to deliver an accurate solution to the discretized equations representing the laboratory flows, the discrepancies in the observed and simulated residual currents were assumed to arise from one (or both) of two sources. First, it is possible that spatial resolution – e.g., of the important bottom boundary layers at the coastal floor – is insufficient in E1. Second, the assumed physical equations, which are themselves approximate by virtue of several large- and grid-scale assumptions (e.g., hydrostatic balance, linear Ekman bottom stress law, etc.) may be the source of some of the experiment-model differences observed by Perenne et al. Experiments E2 and E3 have since been conducted to assess these alternatives.

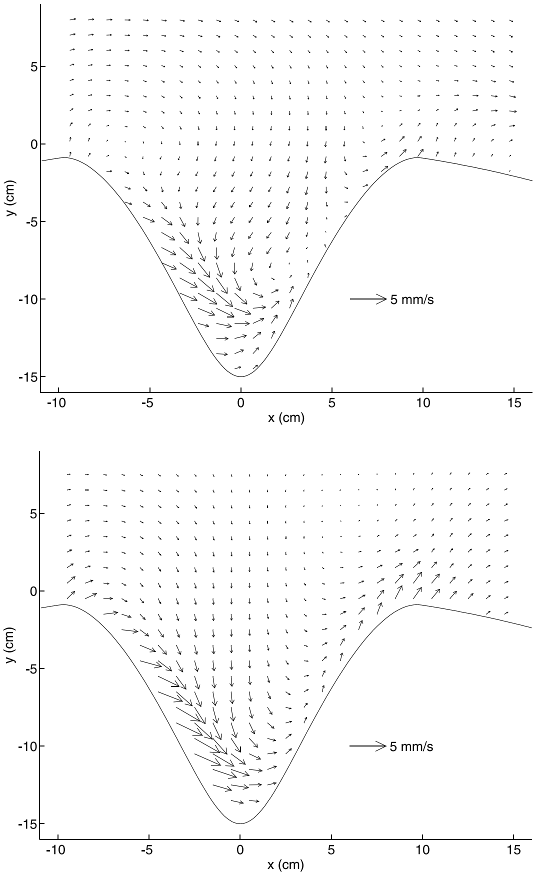

Fig. 8. Residual flow in the laboratory (top figure) and in numerical experiment E1 (lower figure) at the shelf-break level ($z = 0.025$ m).

The residual vorticity and divergence fields given by all three numerical experiments, as well as the laboratory model, are shown in Figs. 9 and 10. Note in particular that whereas simulation E1 produces a convergence area stretched along the upstream wall, the convergence observed in the laboratory occurs in a more centralized area near the head of the canyon. The more highly resolved, no-slip exeriments (E2, E3) by contrast have a more localized region of convergence aligned over the axis of the canyon, as in the laboratory measurements. Although laboratory estimates of vorticity and divergence are lacking close to the canyon sidewalls (and thus do not accurately define the sidewall boundary layers), it seems visually apparent that the no-slip numerical experiments have overly thick sidewall layers. (This is unsurprising, since they were conducted with larger than molecular values of viscosity.) As a consequence, the central region of negative divergence is "squeezed outwards" along the canyon axis relative to the laboratory estimates. Nonetheless, overall structural and quantitative agreement with the laboratory vorticity and divergence fields is clearly improved greatly by the introduction of the "true" no-slip bottom boundary condition. It is not obvious from these figures, however, whether the reduction in the value of horizontal viscosity in E3 produced any positive improvement. This raises the question as to whether lower values of subgridscale mixing coefficients, higher space/time resolution, and the correct (no-slip) bottom boundary condition would be sufficient in themselves to eventually achieve agreement with the laboratory measurements to within the limits of measurement error.

[redacted]

on was ob-
cials, another
he structure of
to boundary
s er feature
s er to be
y tic as-
d
ra odels
g a t in
m the
r, i le

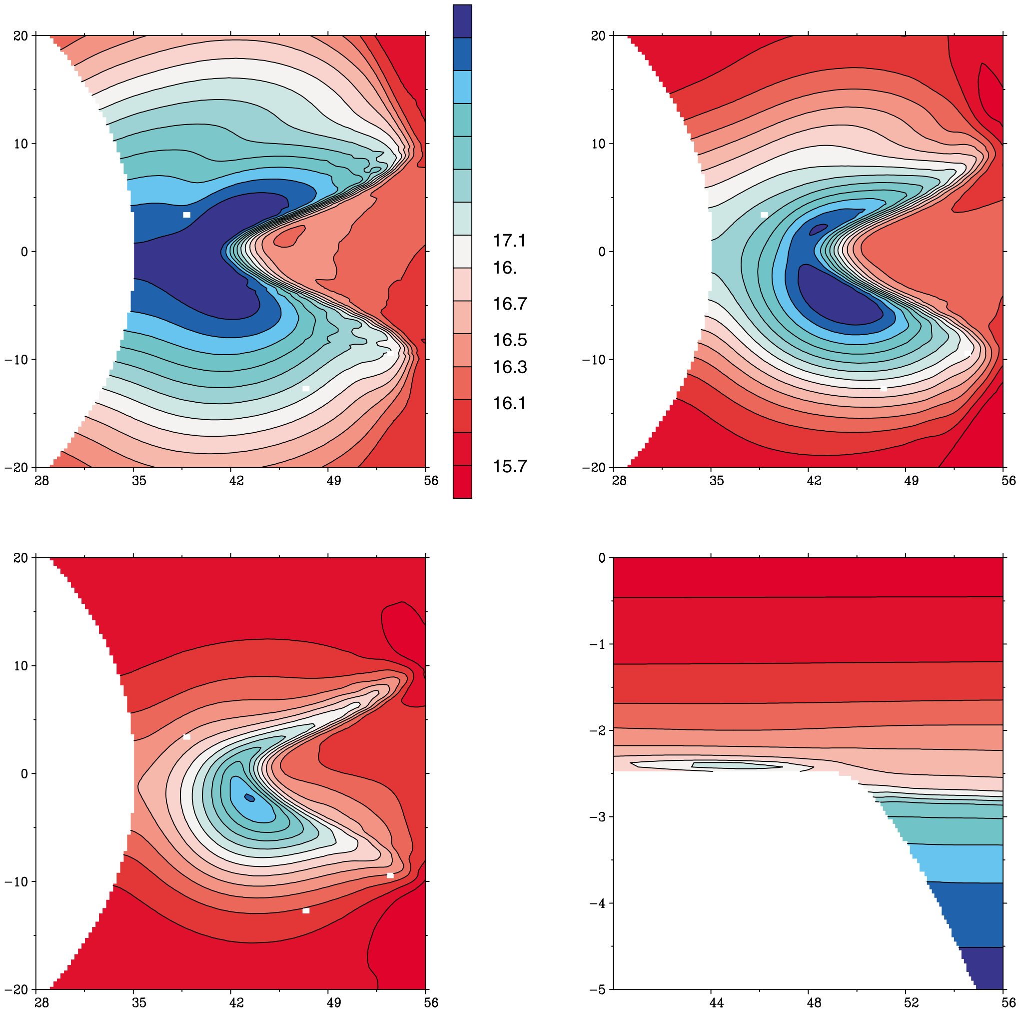

that only a non-hydrostatic simulation would materially improve the comparisons further. A non-hydrostatic version of SEOM is under development to explore just such questions.

12. Parallelization

The spectral element method is often characterized as a coarse-grained algorithm since heavy computations need to be performed before inter-element communication is required. An order-of-magnitude analysis shows that the speed-up in a typical two-dimensional application is:

$$S = \frac{P}{1 + (T_c/KT_o)}, \quad \frac{T_c}{KT_o} \sim \frac{1}{\sqrt{K}\mathrm{O}(N^2)}, \tag{67}$$

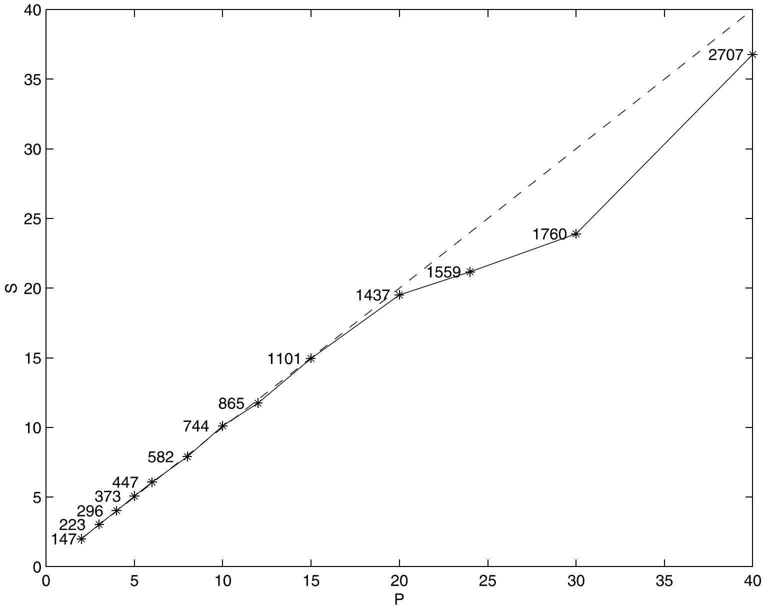

Fig. 12. Speed-up as a function of processor number on CRAY-T3E 600. The speed-up is defined as the ratio T_p/T_1, where T_p is the CPU time needed to compute a single time-step for a fixed-size problem. The dashed line represents the ideal linear speed-up. The numbers represent MFLOPS rates.

where P is the number of processors, K the number of spectral element within each processor, N the spectral truncation, T_o is the computational time, and T_c is the communication time. The above formula shows that the speed-up deteriorates as the second term in the denominator increases. This second term decreases quadratically with the spectral truncation, and like the square root of the number of elements in the partition. The formula also shows the distinguishing property of the spectral element method which gives it its coarse-grain character: the communication cost increases only linearly with the order of the method while its computational cost increases cubically, yielding a quadratic ratio between the two. High-order finite difference methods, by contrast, show a quadratic increase of the communication cost with the order, since the number of halo points needed to be passed between processors increases.

The good scalability characteristics of the spectral element model are illustrated in the speed-up and MFLOPS curves shown in Fig. 12. The computations consist of simulating the oceanic circulation in the North-Atlantic Basin using the grid shown in Fig. 1. These performance curves were obtained on a CRAY-T3E, after removing the initialization cost. The peak measured floating-point operation count is 2.7 GFLOPS on 40 processors, reflecting a per-processor speed of about 67.5 MFLOPS.

The parallelization is based on a static decomposition of the grid which is then distributed to the processors. Due to the irregularity of the grid and the decomposition, we have adopted a message passing implementation that allows precise control over the data decomposition and the overlapping of communications and computations. The explicit message-passing approach also frees us from relying on compiler sophistication.

13. Discussion

We have presented a spectral element model for the solution of the Boussinesq and hydrostatic Navier–Stokes equations. This model relies on a spectral element discretization in all three directions. These grids are allowed to be unstructured in the horizontal, but are restricted to a constant number of elements in the vertical at the present time. The vertical partition can be adjusted so as to emphasize arbitrary depth levels. The model is terrain-following in that the deepest element follows the shape of the bathymetry.

The model features a free surface whose update is treated separately from the rest of the calculation, and via the solution of two-dimensional, and shallow water like, equations. We have the choice of integrating these equations implicitly with a time step synchronous with the three-dimensional equations, or split-explicit with a small step that respects the CFL condition on the fast gravity modes followed by a long integration step on the three-dimensional fields.

Vertical mixing schemes are necessary in hydrostatic models in order to prevent unstable stratification, i.e., stratification where higher density fluid is sitting atop lighter fluid. These situations are unlikely to occur in nature since any small perturbation will cause the heavy fluid parcel to accelerate downward, acceleration that is omitted in the hydrostatic momentum equations. We have implemented various mixing parameterizations in our simulations, either based on buoyancy frequency parameterization or on the Richardson number stability criterion. Both parameterizations work by increasing the vertical viscosity coefficient in order to enhance the vertical mixing process and return the fluid to a state of stable stratification. The code currently uses the KPP parameterization of Large et al. [12].

The model presented herein has been applied to various test problems in the idealized and process-oriented limits. The baroclinic Kelvin wave problem shows that the model retains its spectral convergence properties. The gravitational adjustment problem highlights the ability of the model to deal with frontogenesis when care is taken to keep the front resolved, i.e., keeping its width larger than the spacing between two collocation points. Finally the model results compare qualitatively well to the laboratory experiments on flow rectification near a submarine canyon. The monograph of Haidvogel and Beckmann [7] contains more idealized test problems and evaluates the performance of the present model as well as other well-known ocean models.

We are currently in the process of revisiting some aspects of our model prior to presenting realistic tests. Specifically, we are experimenting with the Discontinuous Galerkin Method (DGM, see [3,11,15] for more details), for the tracer evolution equations. DGM is better suited for advection dominated problems, and has several advantages over the "classical" formulation presented here. The most attractive features of DGM in the context of geophysical simulations are: enforcement of element-wise conservation, and the use of discontinuous finite elements. The latter property will, among other things, allow an easier implementation of p-adaptivity for the tracer, as well as open the possibility to staggering the vertical velocity and tracer collocation points.

Acknowledgements

This research was supported by the office of Naval Research under Grant No. N00014-93-1-0197, by the National Science Foundation under Grants OCE-9632809, OCE-9619780, OCE-9730596, and ACI-9814651. This work was supported in part by a grant of HPC time from the Arctic Region Supercomputing Center. Additional computational resources were provided by the Naval Oceanographic Office/MSRC Program, NAVO. We would like to thank Dr. Chris Edwards for adding the KPP-mixing parameterization, as well as the anonymous reviewers whose comments and suggestions lead to substantial improvements in the manuscript.

Appendix A. Depth-averaged equations

The vertical integral of the continuity equation takes the form:

$$\int_{-h}^{\zeta} \nabla \cdot \mathbf{u} \, \mathrm{d}z + w|_{z=\zeta} - w|_{z=-h} = 0. \tag{A.1}$$

Leibnitz's theorem is used to pull out the horizontal divergence term out of the integral and obtain:

$$\nabla \cdot \left(\int_{-h}^{\zeta} \mathbf{u}\,\mathrm{d}z \right) + (w|_{\zeta} - \mathbf{u}|_{\zeta} \cdot \nabla\zeta) - (w|_{-h} + \mathbf{u}|_{-h} \cdot \nabla h) = 0. \tag{A.2}$$

The surface and bottom kinematic boundary conditions are invoked to eliminate the second and third term in the above equation. Using the definition of the depth-averaged velocity we obtain the depth-averaged continuity equation (13).

The derivation of the depth-averaged momentum equation is a little bit more intricate, and we proceed by looking at individual terms in the equations. It is first useful to write the acceleration term as

$$\frac{D\mathbf{u}}{Dt} = \frac{\partial \mathbf{u}}{\partial t} + \nabla \cdot (\mathbf{u}\mathbf{u}) + \frac{\partial w\mathbf{u}}{\partial z} \tag{A.3}$$

after invoking the continuity equation. The first term on the right-hand side of (A.3) is the local acceleration and the second is the advective acceleration. Vertical integration of the acceleration leads to

$$\frac{\partial (h+\zeta)\mathbf{U}}{\partial t} + \nabla \cdot \left(\int_{-h}^{\zeta} \mathbf{u}\mathbf{u}\,\mathrm{d}z \right) - \left[\mathbf{u} \left(\frac{\partial \zeta}{\partial t} + \mathbf{u} \cdot \nabla\zeta - w \right) \right]_{z=\zeta} - [\mathbf{u}(\mathbf{u} \cdot \nabla h + w)]_{z=-h} \tag{A.4}$$

after interchanging the order of integration and differentiation. The third and fourth terms of (A.4) vanish by virtue of the kinematic boundary conditions at the top and bottom surfaces. We now break up the velocity in the second term in Eq. (A.4) as $\mathbf{U} + (\mathbf{u} - \mathbf{U})$; the term in parenthesis has zero depth average by definition. Substituting this expression in the second term in Eq. (A.4) and evaluating the integrals we arrive at:

$$(h+\zeta)\left(\frac{\partial \mathbf{U}}{\partial t} + \mathbf{U} \cdot \nabla \mathbf{U} \right) + \nabla \cdot \left(\int_{-h}^{\zeta} (\mathbf{u} - \mathbf{U})(\mathbf{u} - \mathbf{U})\,\mathrm{d}z \right) + \mathbf{U} \left\{ \frac{\partial \zeta}{\partial t} + \nabla \cdot [(h+\zeta)\mathbf{U}] \right\}. \tag{A.5}$$

The depth-averaged continuity equation can now be invoked to eliminate the last term in the above expression. The integral in (A.4) represent the depth average of the nonlinear interaction of baroclinic velocities.

Vertical integration of the Laplacian dissipation leads to:

$$\nabla \cdot \left(\int_{-h}^{\zeta} \alpha \nabla u\,\mathrm{d}z \right) + (-\alpha \nabla u \cdot \nabla\zeta + v\mathbf{u}_z)|_{\zeta} + (-\alpha \nabla u \cdot \nabla h - v\mathbf{u}_z)|_{-h}. \tag{A.6}$$

Note that the outward unit normal at the sea surface and the sea bed are given by:

$$\mathbf{n}|_{\zeta} = \frac{1}{(1 + |\nabla\zeta|^2)^{1/2}}(-\nabla\zeta + \mathbf{k}), \tag{A.7}$$

$$\mathbf{n}|_{-h} = \frac{1}{(1 + |\nabla h|^2)^{1/2}}(-\nabla h - \mathbf{k}). \tag{A.8}$$

Hence, the second and third terms in Eq. (A.6) are nothing but the product of the friction force in the x-direction with a vector parallel to the outward unit normal. Using the stress boundary conditions we arrive at

$$\nabla \cdot \left(\int_{-h}^{\zeta} \alpha \nabla u\,\mathrm{d}z \right) + \tau (1 + |\nabla\zeta|^2)^{1/2} - \gamma \|\mathbf{u}\| u (1 + |\nabla h|^2)^{1/2}. \tag{A.9}$$

The metric terms appearing next to the bottom and surface stresses arise because of the curvature of the bounding surfaces.

The integration of the various linear terms is straightforward, the final form of the depth-averaged momentum equation, after division by the total depth, is given in Eq. (14). The expressions for **C** and **D** are given by

$$\mathbf{C} = \frac{1}{h+\zeta}\nabla\cdot\left[\int_{-h}^{\zeta}(\mathbf{u}-\mathbf{U})(\mathbf{u}-\mathbf{U})\,\mathrm{d}z\right] + \frac{1}{h+\zeta}\int_{-h}^{\zeta}\nabla p\,\mathrm{d}z, \tag{A.10}$$

$$\mathbf{D} = \frac{1}{h+\zeta}\nabla\cdot\left(\int_{-h}^{\zeta}\alpha\nabla\mathbf{u}\,\mathrm{d}z\right). \tag{A.11}$$

Appendix B. Errors due to mapping between physical space and computational space

For the simple geometry shown in Fig. 3, the map from computational to physical space in the kth element from the surface is

$$x = L\frac{\xi+1}{2}, \quad z = \frac{h}{K}\left(\frac{\sigma+1}{2}-k\right), \tag{B.1}$$

where $h(\xi)/K$ is the horizontally varying height of an element. For this particular case, the only non-zero metric terms are

$$\begin{aligned} x_\xi &= \frac{L}{2}, \\ z_\xi &= \frac{h_\xi}{K}\left(\frac{\sigma+1}{2}-k\right) \quad z_\sigma = \frac{h}{2K}. \end{aligned} \tag{B.2}$$

For a rectangular element the mapping from x to ξ space can be represented exactly, and hence $\|\bar{x}_\xi - x_\xi\| = 0$. The error in representing z_ξ, and subsequently σ_x, depends essentially on how well the bathymetry is represented; we have:

$$\|\bar{z}_\xi - z_\xi\| \leqslant \frac{\|h_\xi - \bar{h}_\xi\|}{K}\max_{k,\sigma}\left(\frac{\sigma+1}{2}-k\right), \tag{B.3}$$

$$\|\bar{z}_\xi - z_\xi\| \leqslant \frac{\|h_\xi - \bar{h}_\xi\|}{K}. \tag{B.4}$$

Hence the 2-norm of the slopes can be bounded by [2]:

$$\|\bar{z}_\xi - z_\xi\|_2 \leqslant AN^{((5/2)-m)}\|h\|_{H^m}. \tag{B.5}$$

Here N is the degree of the polynomial interpolating the depth h, A is a positive constant, and $\|h\|_{H^m}$ is the Sobolev norm [2] of the depth. The latter is essentially a measure of the smoothness of h. We now turn our attention to the σ_x term. Since $\sigma_x = (-z_\xi)/z_\sigma x_\xi$, we have

$$\|\bar{\sigma}_x - \sigma_x\| = \frac{-\bar{z}_\xi}{\bar{z}_\sigma\bar{x}_\xi} - \frac{-z_\xi}{z_\sigma x_\xi} \tag{B.6}$$

$$= -\frac{\bar{z}_\xi - z_\xi}{\bar{z}_\sigma\bar{x}_\xi} + \frac{z_\xi}{z_\sigma\bar{z}_\sigma x_\xi}(\bar{z}_\sigma - z_\sigma) + \frac{z_\xi}{\bar{z}_\sigma\bar{x}_\xi x_\xi}(\bar{x}_\xi - x_\xi). \tag{B.7}$$

The last term in our case is zero and we can write

$$\|\bar{\sigma}_x - \sigma_x\|_2 \leqslant \left\|\frac{1}{\bar{z}_\sigma \bar{x}_\xi}\right\|_2 \|\bar{z}_\xi - z_\xi\|_2 + \left\|\frac{1}{z_\sigma \bar{z}_\sigma x_\xi}\right\|_2 \|z_\xi\|_2 \|\bar{z}_\sigma - z_\sigma\|_2 \tag{B.8}$$

$$\leqslant \frac{2}{L}\left\|\frac{2K}{h}\right\|_2 \|\bar{h}_\xi - h_\xi\|_2 + \frac{2}{L}\left\|\frac{4K^2}{h\bar{h}}\right\|_2 \|h_\xi\|_2 \frac{\|\bar{h} - h\|_2}{2K}. \tag{B.9}$$

We have the following result concerning the interpolation and differentiation errors of Legendre polynomials:

$$\|\bar{h} - h\|_2 \leqslant BN^{(1/2)-m}\|h\|_{H^m}, \tag{B.10}$$

$$\|\bar{h}_\xi\|_2 \leqslant CN^2\|h\|_2, \tag{B.11}$$

B and C are positive constants. Furthermore, we can bound the 2-norm with the maximum norm to get

$$\|h\|_2 \leqslant Dh_{\max}, \quad \left\|\frac{1}{h}\right\|_2 \leqslant E\frac{1}{h_{\min}}, \quad \left\|\frac{1}{\bar{h}}\right\|_2 \leqslant F\frac{1}{h_{\min}}, \tag{B.12}$$

where D, E, and F are positive constants. Finally, we have the following bounds on the σ_x error

$$\|\bar{\sigma}_x - \sigma_x\|_2 \leqslant Q\frac{1}{h_{\min}}\left[1 + R\frac{h_{\max}}{h_{\min}}\right]N^{((5/2)-m)}\|h\|_{H^m}. \tag{B.13}$$

The above expression shows that the error in the vertical mapping depends on the smoothness of the topography, the degree of the polynomial N used to interpolate the depth, and on the ratio of the depth excursion within a single element. Furthermore, the bound on the error decreases spectrally for an infinitely smooth topography.

References

[1] J.P. Boyd, Chebyshev and Fourier Spectral Methods, Lecture Notes in Engineering, Springer, New York, 1989.

[2] C. Canuto, M.Y. Hussaini, A. Quarteroni, T.A. Zang, Spectral Methods in Fluid Dynamics, Springer Series in Computational Physics, Springer, New York, 1988.

[3] B. Cockburn, An introduction to the discontinuous Galerkin method for convection dominated flows, in: A. Quarteroni (Ed.), Advanced Numerical Approximation of Nonlinear Hyperbolic Equations, Springer, New York, 1998, pp. 151–268.

[4] E.N. Curchitser, D.B. Haidvogel, M. Iskandarani, On the transient adjustment of a mid-latitude abyssal ocean basin with realistic geometry: The constant depth limit, Dynamics of Atmosphere and Oceans 29 (2–4) (1999) 147.

[5] E.N. Curchitser, D.B. Haidvogel, M. Iskandarani, On the transient adjustment of a mid-latitude abyssal ocean basin with realistic geometry and bathymetry, Journal of Physical Oceanography 31 (3) (2001) 725.

[6] E.N. Curchitser, M. Iskandarani, D.B. Haidvogel, A spectral element solution of the shallow water equations on multiprocessor computers, Journal of Atmospheric and Oceanographic Technology 15 (2) (1998) 510–521.

[7] D.B. Haidvogel, A. Beckmann, Numerical Ocean Circulation Modeling, Imperial College Press, 1999.

[8] D.B. Haidvogel, E. Curchitser, M. Iskandarani, R. Hughes, M.A. Taylor, Global modeling of the ocean and atmosphere using the spectral element method, Atmosphere-Ocean 35 (1997) 505–531.

[9] R.L. Higdon, A.F. Bennett, Stability analysis of operator splitting for large-scale ocean modeling, Journal of Computational Physics 123 (2) (1996) 311.

[10] M. Iskandarani, D.B. Haidvogel, J.P. Boyd, A staggered spectral element model with application to the oceanic shallow water equations, International Journal for Numerical Methods in Fluids 20 (1995) 393–414.

[11] G.E.M. Karniadakis, S.J. Sherwin, Spectral/hp Element Methods for CFD, Oxford University Press, Oxford, 1999.

[12] W.G. Large, J.C. McWilliams, S.C. Doney, Oceanic vertical mixing: a review and a model with a non-local boundary layer parameterization, Reviews in Geophysics 32 (1994) 363–403.

[13] J. Levin, M. Iskandarani, D.B. Haidvogel, A spectral filtering procedure for eddy-resolving simulations with a spectral element ocean model, Journal of Computational Physics 137 (1) (1997) 130–154.

[14] J. Levin, M. Iskandarani, D.B. Haidvogel, A nonconforming spectral element ocean model, International Journal for Numerical Methods in Fluids 34 (6) (2000) 495–525.

[15] I. Lomtev, R.M. Kirby, G.E. Karniadakis, A discontinuous Galerkin ale method for compressible viscous flows in moving domains, Journal of Computational Physics 155 (1) (1999) 18–159.

[16] H. Ma, A spectral element basin model for the shallow water equations, Journal of Computational Physics 109 (1993) 133–149.

[17] N. Perenne, D.B. Haidvogel, D.L. Boyer, Laboratory–numerical model comparisons of flow over a coastal canyon, Journal of Atmospheric and Oceanographic Technology 18 (2001) 235–255.

[18] Y.H. Song, A general pressure gradient formulation for ocean models. part *1*: Scheme design and diagnostic analysis, Monthly Weather Review 126 (1) (1998) 3213–3230.

[19] Y.H. Song, D.B. Haidvogel, A semi-implicit ocean circulation model using a generalized topography-following coordinate system, Journal of Computational Physics 105 (1) (1994) 228.

[20] M.A. Taylor, R. Loft, J. Tribbia, Performance of a spectral element atmospheric model (seam) on the hp exemplar spp2000, Technical Report NCAR/TN-439 + EDD, National Center for Atmospheric Research, Boulder, CO, 1998.

[21] M.A. Taylor, J. Tribbia, M. Iskandarani, The spectral element method for the shallow water equations on the sphere, Journal of Computational Physics 130 (1) (1997) 92–108.

[22] M.A. Taylor, B.A. Wingate, A generalized diagonal mass matrix spectral element method for non-quadrilateral elements, Applied Numerical Mathematics 33 (1/4) (2000) 259.

[23] M.A. Taylor, B.A. Wingate, R.E. Vincent, An algorithm for computing fekete points in the triangle, SIAM Journal on Numerical Analysis 33 (5) (2000) 1707–1720.

[24] D.-P. Wang, Mutual intrusion of a gravity current and density front formation, Journal of Physical Oceanography 14 (1984) 1191–1199.

[25] D.L. Williamson, J.B. Drake, J.J. Hack, R. Jakob, P.N. Swarztrauber, A standard test set for the numerical approximations to the shallow water equations in spherical geometry, Journal of Computational Physics 102 (1992) 211–224.

[26] B.A. Wingate, J.P. Boyd, Spectral element methods on triangles for geophysical fluid dynamics problems, In: Proceedings of the Third International Conference On Spectral and High-order Methods, Houston, Texas, 1996, pp. 305–314, Houston Journal of Mathematics.

[27] C. Wunsch, D.B. Haidvogel, M. Iskandarani, R. Hughes, Dynamics of the long-period tides, Progress in Oceanography 40 (1/4) (1997) 80–108.